

Article

The Convective Heat Transfer Performance and Structural Optimization of the Cavity in Energy-Saving Thermal Insulation Windows under Cold Air Penetration Condition

Zhiqiang Wang ^{1,2} , Qi Tian ^{1,*} and Jie Jia ¹

¹ Department of Building Environment and Energy Application Engineering, Taiyuan University of Technology, Yingze Street No. 209, Taiyuan 030024, China; wangzhiqiang0081@link.tyut.edu.cn (Z.W.); jiajie@tyut.edu.cn (J.J.)

² Department of Environment and Safety Engineering, Taiyuan Institute of Technology, Xinlan Road No. 31, Taiyuan 030008, China

* Correspondence: tianqi@tyut.edu.cn

Abstract: In buildings with the solar heat collection/insulation energy-saving window (SHC/IESW), when the insulation device is placed at night in winter, a double-wall structure façade (DSF) is formed between the glass and the insulation curtain, and the existence of air inlet and outlet leads to cold air penetration. In this paper, the Nusselt number (Nu) correlation and convective heat transfer coefficient (CHTC) of the cavity in SHC/IESW were calculated through an experiment combined with a theoretical analysis. Then, numerical simulation was performed on the fluid dynamics and thermal characteristics caused by air convection in an asymmetrically heated cavity under uniform heat flow conditions, to optimize the SHC/IESW structure and analyze its heat transfer mechanism to solve the problem of convection heat transfer between plates under cold air infiltration. Using the calculation formulas obtained from the experiment, the heat transfer coefficient of SHC/IESW is $1.71 \text{ W}\cdot\text{m}^{-2}\cdot\text{K}^{-1}$. The numerical simulation results showed that with the increase of air layer thickness, the outlet temperature, the average air velocity of the cavity, and the surface temperature of thermal insulation curtain all decrease; with the increase of inlet width, the outlet temperature and the surface temperature of thermal insulation curtain decreases significantly, while the average air velocity of cavity increases. It can help to weaken the convective heat transfer in the cavity and thus, reduce the total heat transfer coefficient to $1.28 \text{ W}\cdot\text{m}^{-2}\cdot\text{K}^{-1}$ when the air layer thickness is 12 mm and the inlet width is 1 mm.

Keywords: convective heat transfer coefficient; optimized double-wall structure façade; asymmetric heated cavity; cold air penetration condition



Citation: Wang, Z.; Tian, Q.; Jia, J. The Convective Heat Transfer Performance and Structural Optimization of the Cavity in Energy-Saving Thermal Insulation Windows under Cold Air Penetration Condition. *Energies* **2022**, *15*, 2481. <https://doi.org/10.3390/en15072481>

Academic Editor: Fabrizio Ascione

Received: 22 February 2022

Accepted: 25 March 2022

Published: 28 March 2022

Publisher's Note: MDPI stays neutral with regard to jurisdictional claims in published maps and institutional affiliations.



Copyright: © 2022 by the authors. Licensee MDPI, Basel, Switzerland. This article is an open access article distributed under the terms and conditions of the Creative Commons Attribution (CC BY) license (<https://creativecommons.org/licenses/by/4.0/>).

1. Introduction

At present, building energy consumption accounts for nearly about 40% of the total social energy consumption, and the energy consumption from the heat transfer process of windows accounts for about 30% of the building energy consumption. Previous studies [1,2] proposed a solar heat collection/insulation energy-saving window (SHC/IESW) for nighttime insulation and daytime heat gain in winter, and sunshade and nighttime heat dissipation in summer. To reduce heat transfer from inside to outside in the winter night, the thermal insulation curtain is placed, a cavity structure with cold air permeating between the curtain and the glass is formed, which is part of a double-skin façade (DSF) structure.

DSF is a multi-layer skins construction with an external skin, a cavity, and an inner skin, in which the external and internal skins could be of either glass or other materials [3,4]. The DSF's heat transfer performance depends closely on the chosen ventilation mode within its intermediate space [5–9], so the convective heat transfer problem in the cavity is the key to analyzing the thermal insulation efficiency of the structure during winter nights.

Several experimental and theoretical studies concerning the thermal performance of the cavity between DSF layers mentioned the calculation of the convective heat transfer coefficient (CHTC) [10–16]. However, few studies use experimental methods combined with heat balance calculation to accurately deduce the Nusselt number (N_u) correlations and the CHTC.

Cipriano et al. [17] introduced a methodology to analyze the valid range of the existing mathematical correlations for the CHTCs in laminar and the transition to turbulent free convection. Ioannidis et al. [18] experimentally developed the average N_u number correlations for air flow in DSF with the Semi-Transparent Photovoltaics (STPV) using a full-scale outdoor test facility. The heat loss of a typical building is about 20% higher than that of a building that integrates DSF-STPV. Agathokleous et al. [19] reviewed various N_u number correlations and CHTCs, from previous studies, under several assumptions and conditions.

Inan et al. [20] constructed a non-dimensional correlation between Reynolds (R_e) and N_u numbers to evaluate the heat transfer performance of the cavity. Kim et al. [21] presented open channel natural convection with separated boundary conditions, in which the CHTCs were evaluated numerically while the channel inlet was assigned to a fully developed velocity profile at a constant temperature. Guo et al. [22] investigated the heat transfer of night ventilation with diffuse ceiling ventilation (DCV) concept in an office room. New correlations based on experimental CHTCs were developed for potential application in building energy simulation tools.

Cuevas et al. [23] proposed an empirical model to determine the convective heat loss at an indoor glazing surface, which allowed the calculation of the CHTC and the air flow rate entering the window cavity formed between the glazing surface and the protection device. Buonomo et al. [24] numerically investigated the transient natural convection in the parallel-plate vertical microchannel to evaluate their effects on wall temperatures, mass flow rate, velocity profiles, and N_u number.

Other studies focused on the cavity's temperature or the cavity's air velocity field in the DSF structure [25–31]; however, limited studies used a simulation analysis method to carefully analyze the temperature field inside the cavity under different structural parameters to achieve the optimization of detailed structure.

Lau et al. [32] explored the effect of varying the inclination angle on the velocity and temperature fields, and the results showed that open-ended channels with low inclination angles are characterized by low chimney effect and induced flow rate, thereby decreasing the heat transfer along with the photovoltaic panels. Souza et al. [33] investigated the efficiency of a naturally ventilated DSF built, and the results showed that the DSF contributed to a decrease in the temperature inside the environment because it inhibits direct solar radiation. Jamal et al. [34] investigated the combined heat transfer by natural convection, conduction, and surface radiation through a double solid wall separated by an air layer. Their results showed that the use of an air layer thickness of 5 cm combined with a low emissivity of the structure surfaces would greatly help in reducing the building energy consumption.

Other researches [35–37] emphasized the flow velocity inside the channel and an optimal air supply control for a DSF or the air temperatures in an easy-to-open 270 mm slim-type double skin window, to analyze the most optimal effects on cooling energy reductions.

The previously mentioned studies had extensively explored the heat transfer performance and temperature field of the DSF structure, and many valuable conclusions have been drawn. However, fewer studies systematically derived the N_u number correlation and CHTC through experiments combined with heat balance calculation; No study uses simulation analysis methods to evaluate the DSF performance under different structural parameters to achieve the optimization of detailed structure.

This paper presents a special study on the CHTC in the cavity under the penetration of cold air by means of experiment and numerical simulation, obtains the N_u number

correlation formula suitable for this model; and numerically analyzes the temperature field inside the cavity under different structural parameters to achieve the optimization of the detailed structure, which can enlarge the large-scale application of SHC/IESW. Before the formal simulation, the numerical model is validated through experimental test data, whose dimensions correspond to the model.

2. Materials and Methods

2.1. Study Experiment

2.1.1. Experiment Platform

The experimental procedure is carried out mainly in a DSF, which is composed of a 6 mm glass and a thermal insulation curtain, and a cavity between both. Cold air enters the storage box from the air inlet, passes through the cavity, and finally exits from the outlet. The size of the experiment platform is shown in Figure 1, and the construction materials and properties are presented in Table 1.

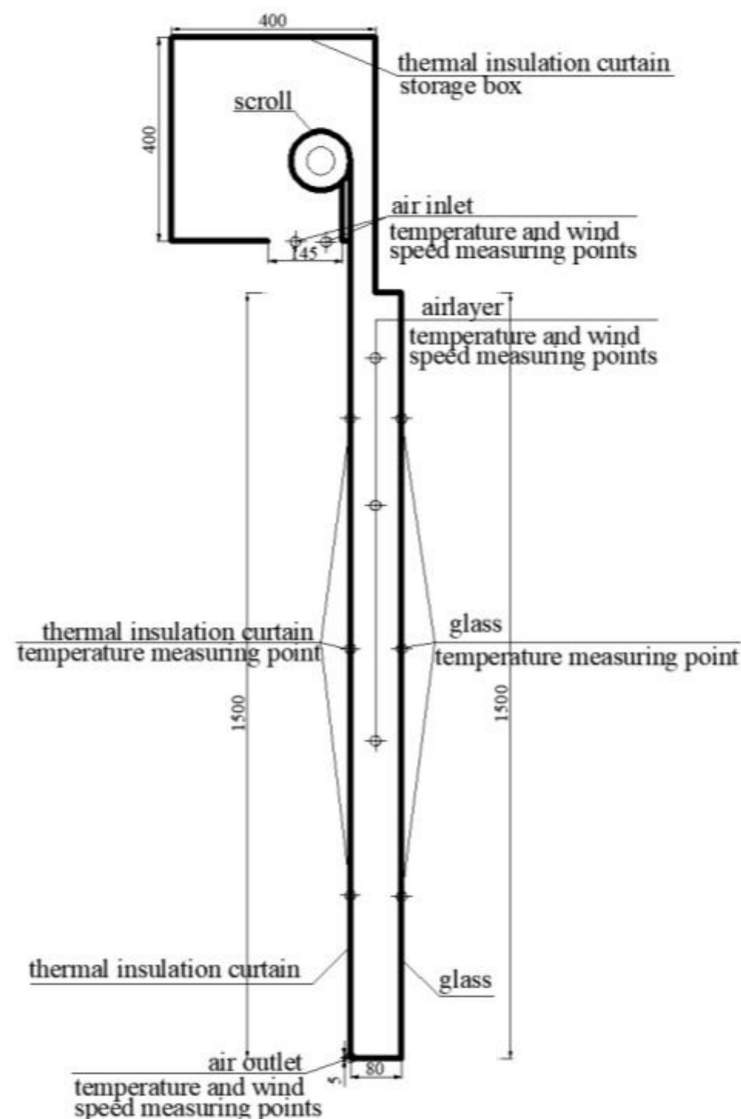


Figure 1. Experimental determination of the layout.

The thermal insulation curtain device is composed of a curtain, a curtain storage box, and a curtain guide rail. The curtain is filled with a 2 cm thick polyurethane aluminum alloy shell connected to each other.

Table 1. Structure parameters of the DSF.

Item	SHC/IESW
Installation position of thermal insulation device	Outside
Thickness of thermal insulation curtain (δ)/cm	2
Thermal conductivity of thermal insulation curtain/($W \cdot m^{-1} \cdot K^{-1}$)	0.10
Thickness of cavity (d)/cm	8
Thermal conductivity of glass/($W \cdot m^{-1} \cdot K^{-1}$)	0.77
Glass thickness/m	0.006
Air inlet dimension/mm	145 (W) \times 1400 (L)
Air outlet dimension/mm	10 (W) \times 1400 (L)
Storage box width/mm	430
Storage box length/mm	1400

2.1.2. Instruments

Several PT100 thermal resistance temperature sensors are installed for temperature measurement: three sensors on the inner face of the glass, three on the inner face of the thermal insulation curtain, two on the inlet of the cavity, two on the outlet of the cavity, and three in the middle of the cavity, which has an air layer thickness of 0.1 m.

Furthermore, Test410-1 hot wire anemometers are positioned to obtain the air velocity in the inlet and outlet of the cavity. Figure 1 also lists the locations of the measure points, and Table 2 lists the specifications of the main instruments.

Table 2. Specifications of the main instruments.

Equipment	Type	Parameters
PT100 thermal resistance temperature sensor	WZPK333	Range: -200 – 600 °C; resolution: 0.1 °C
Heat flow meter	JTSOFT-METER	Range: 0 – 2000 $W \cdot m^{-2}$; resolution: 0.1 $W \cdot m^{-2}$
Anemometer	TESTO410-1	Range: 0.4 – 20 $m \cdot s^{-1}$; resolution: 0.1 $m \cdot s^{-1}$

2.1.3. Experimental Instrument Check

To ensure the reliability of the experimental results, the accuracy of the instruments needed in the experiment must be checked. Therefore, uncertainty analysis and error analysis were carried out for the three instruments used above.

Liquid with a fixed temperature of 15 °C, a solid wall with a fixed heat flow of 50 $W \cdot m^{-2}$, and a place with a fixed wind speed of 3 $m \cdot s^{-1}$ were selected, respectively. The temperature sensor, flowmeter, and anemometer were used to measure them 10 consecutive times, and then the values were read and analyzed as below.

- (1) Uncertainty Analysis Instrument uncertainty can be expressed as U or U_r . In the table below, X_i is for the measured values, \bar{X} for the average value, U_r for the relative standard uncertainty, U for the standard uncertainty, S for the standard deviation, Δ_I for the apparatus error, generally calculated by half of the minimum indexing of the instrument.
- (2) Error Analysis Instrument error can be expressed as X_a or X_r . In the table below, X_i is for the measured values, X_t for the true value, X_a for the absolute error value, X_r for the relative error value.

It can be seen from Tables 3 and 4 that the uncertainty and error of the three instruments meet the standards [37], which can ensure the scientific validity of the experimental results.

Table 3. Uncertainty calculation process.

Resistance Temperature Sensor/°C		Heat Flow Meter/Wm ⁻²		Anemometer/ms ⁻¹	
X_i	$X_i - \bar{X}$	X_i	$X_i - \bar{X}$	X_i	$X_i - \bar{X}$
15.1	-0.01	50.0	-0.03	3.0	-0.03
15.2	0.09	50.1	0.07	3.1	0.07
15.1	-0.01	50.2	0.17	3.1	0.07
15.3	0.19	49.8	-0.23	2.9	-0.13
15.0	-0.11	49.9	-0.13	2.8	-0.23
15.2	0.09	50.1	0.07	3.0	-0.03
14.9	-0.21	50.2	0.17	3.2	0.17
15.1	-0.01	49.9	-0.13	3.2	0.17
15.0	-0.11	50.0	-0.03	3.1	0.07
15.2	0.09	50.1	0.07	2.9	-0.13
$\bar{X} = 15.11$		$\bar{X} = 50.03$		$\bar{X} = 3.03$	
$S = \sqrt{\frac{\sum(X_i - \bar{X})^2}{n-1}} = 0.12$		$S = \sqrt{\frac{\sum(X_i - \bar{X})^2}{n-1}} = 0.13$		$S = \sqrt{\frac{\sum(X_i - \bar{X})^2}{n-1}} = 0.09$	
$\Delta_I = 0.05$		$\Delta_I = 0.05$		$\Delta_I = 0.05$	
$U = \sqrt{S^2 + \Delta_I^2} = 0.13$		$U = \sqrt{S^2 + \Delta_I^2} = 0.14$		$U = \sqrt{S^2 + \Delta_I^2} = 0.10$	
$U_r = \frac{U}{\bar{X}} = 0.86\%$		$U_r = \frac{U}{\bar{X}} = 0.27\%$		$U_r = \frac{U}{\bar{X}} = 3.30\%$	

Table 4. Error calculation process.

Resistance Temperature Sensor/°C			Heat Flow Meter/Wm ⁻²			Anemometer/ms ⁻¹		
X_i	$X_a/°C$	$X_r/\%$	X_i	X_a/Wm^{-2}	$X_r/\%$	X_i	X_a/ms^{-1}	$X_r/\%$
	$X_i - X_t$	$(X_i - X_t)/X_t$		$X_i - X_t$	$(X_i - X_t)/X_t$		$X_i - X_t$	$(X_i - X_t)/X_t$
15.1	0.1	0.7	50.0	0.1	0.2	3.0	0	0.0
15.2	0.2	1.3	50.1	0.2	0.4	3.1	0.1	3.3
15.1	0.1	0.7	50.2	-0.2	-0.4	3.1	0.1	3.3
15.2	0.2	1.3	49.8	-0.1	-0.2	2.9	-0.1	-3.3
15.0	0	0.0	49.9	0.1	0.2	2.8	-0.2	-6.7
15.2	0.2	1.3	50.1	0.2	0.4	3.0	0	0.0
14.9	-0.1	-0.7	50.2	-0.1	-0.2	3.2	0.2	6.7
15.1	0.1	0.7	49.9	0	0.0	3.2	0.2	6.7
15.0	0	0.0	50.0	0.1	0.2	3.1	0.1	3.3
15.2	0.2	1.3	50.1	0.1	0.2	2.9	-0.1	-3.3
$X_t = 15$			$X_t = 50$			$X_t = 3$		
Maximum $X_a = 0.3$			Maximum $X_a = 0.2$			Maximum $X_a = 0.2$		
Maximum $X_r = 1.3\%$			Maximum $X_r = 0.4\%$			Maximum $X_r = 6.7\%$		

2.1.4. Procedure

The experimental procedure is detailed below:

- (1) When measuring the indoor temperature, part of the thermocouple is set on the outer surface of the glass, and three measuring points are set in the vertical direction. The height of the measuring points from the bottom of the glass is 0.4, 0.8, and 1.2 m, respectively, and the horizontal direction is centered. The arrangement of measuring points on the inner surface of the curtain is consistent with that on the outer surface of the glass, which is used to measure the average temperature of the two surfaces, respectively.
- (2) The thermocouple and anemometer are also arranged at the inlet and outlet section to measure the average temperature and wind speed of the inlet and outlet air.
- (3) The thermocouple and anemometer are arranged at three measuring points in the vertical direction. The height of the measuring points from the bottom of the glass is 0.4, 0.8, and 1.2 m, respectively, and the height of the measuring points is in the

middle in the horizontal direction, which is used to measure the air velocity and average temperature of the section.

2.2. Numerical Simulation through Fluent

Fluent is commonly used in the HVAC field, as it can accurately simulate physical phenomena such as air flow, heat transfer, and pollution. Under different conditions, the changes in temperature and velocity in the cavity were numerically examined.

2.2.1. Governing Equations

The governing equations are depicted below according to the assumptions outlined in ANSYS Inc. [38].

The mass Equation:

$$\frac{\partial u}{\partial x} + \frac{\partial v}{\partial x} = 0 \quad (1)$$

The momentum Equation:

$$\frac{\partial}{\partial t}(\rho v) + \nabla \cdot (\rho v v) = -\nabla p + \nabla(\tau) + \rho g + F \quad (2)$$

The energy conservation Equation:

$$\frac{\partial}{\partial t}(\rho h) + \nabla \cdot (\rho h v) = \nabla \cdot [(k + k_t) \nabla T] + S_h \quad (3)$$

where ρ is the density vector; v is the velocity vector; p is the static pressure; τ is the stress tensor; g is the gravitational acceleration; F is other source terms that may arise from resistances or sources, etc.; h is the sensible enthalpy; S_h is the source term that includes any defined volumetric heat sources; k is the molecular conductivity; k_t is the conductivity due to turbulent transport.

The k-epsilon turbulent model was used to resolve the turbulence energy and diffusion rate terms. The details of the terms and constants given in the governing equations can be found in the theory book of ANSYS [38].

2.2.2. Numerical Method

The mathematical simulation model used in this study was operated under the following conditions:

- Air flow conforming to the Boussinesq hypothesis consisted of incompressible flow and steady turbulence.
- Heat dissipation caused by a viscous force and heat storage from the chimney wall were ignored.
- Air leakage was negligible in this model.
- Outdoor environmental parameters, such as outdoor temperature and solar radiation were constants.

The two-equation model was adopted to simulate a turbulence effect in the simulation. To ensure computational accuracy, the discretization schemes for all the variables were second-order upwind schemes. A double algorithm was applied to couple pressure and velocity. The Discrete Ordinates (DO) radiation model was used to calculate the radiant heat transfer between different surfaces. The conservation of mass, momentum, and energy was governed by the Navier-Stokes equations, which were solved using the finite-volume method. The residuals were set at 10^{-4} for the continuity and momentum equations and 10^{-7} for the energy equation.

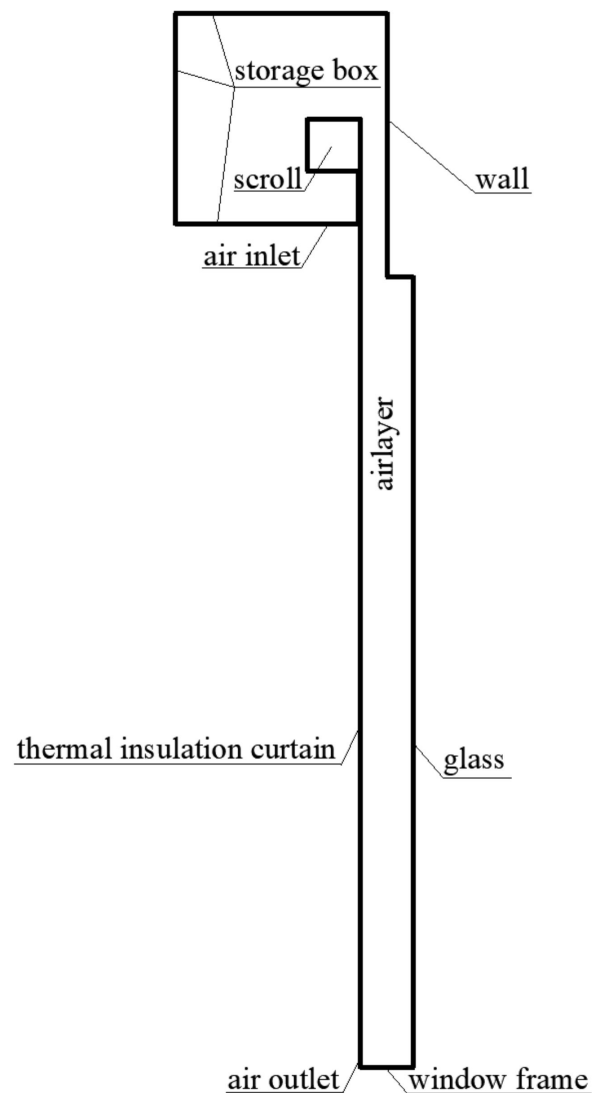
The parameters of the discretization solution are shown in Table 5.

Table 5. The parameters of the discretization solution.

Convergence Criteria	Solution	Variables		
		Pressure	Temperature	Momentum
Flow: 1×10^{-3}	Discretization scheme	second	second	second
	Under-relaxation	0.7	0.3	0.3
Power: 1×10^{-6}	Solving format	AMG	AMG	AMG
	Type of the linear solver	V	flex	flex

2.2.3. Geometrical Setup and Boundary Conditions

A DSF model, shown in Figure 2, was designed with Fluent ICEM Version 10 (ANSYS Inc., Pittsburgh, PA, USA), which is the preprocessing software of the Fluent, and the appearance and size of the model established by the Fluent software and the materials used in the model are completely consistent with the experimental device in Section 2.1.1. The reading section and reading steps of the main indexes are also the same as the layout of the experiment.

**Figure 2.** Model figure.

Meteorological parameters of Taiyuan city, China, were selected in Fluent to simulate the indoor temperature of the room model. Boundary conditions are shown in Table 6.

Table 6. Boundary conditions.

Name	Material	Boundary Type	Heat Transfer Type	Parameter
Glass	Glass	Wall	Constant temperature	290 K
Thermal insulation curtain	Polyurethane	Wall	Constant Heat transfer coefficient (HTC)	23 W/m ² ·K, air temperature: 261.15 K
Storage box	Steel	Wall	Constant flux	Heat insulation
Wall	Insulation board	Wall	Constant flux	Heat insulation
Air inlet	—	Velocity-inlet	Constant flow rate and temperature	5 m/s, 261.15 K, Width: 150 mm
Air outlet	—	outflow	Free outflow	Width: 5 mm

After validation, a series of simulation models were established, focusing on the comparative analysis of the effects of different air inlet widths and different air layer thicknesses on the temperature field between DSF layers.

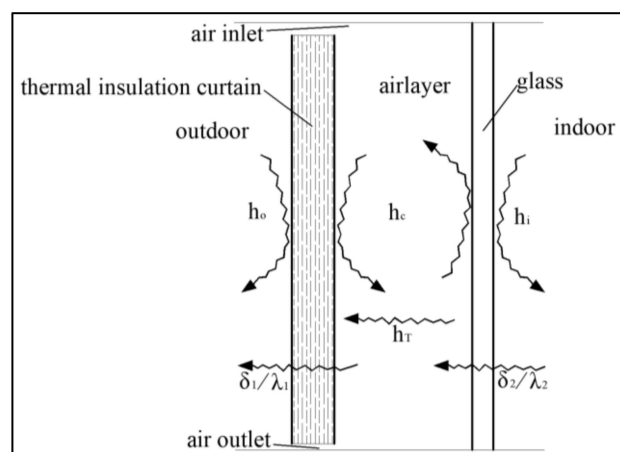
For different air inlet widths, six levels of 1, 5, 10, 50, 100, and 150 mm were set. For different air layer thicknesses, six levels of 2, 4, 6, 8, 10, and 12 cm were set.

3. Results and Discussion

3.1. Heat Transfer Coefficient Calculation through Experimentation

3.1.1. CHTC Calculation Theory and Procedures

Figure 3 shows the calculation diagram of convective heat transfer in air interlayer under the condition of cold air penetration. The SHC/IESW heat transfer process consists of the following: (1) convection on the outside of the curtain, (2) convection on the outside of the glass, (3) heat transfer of the curtain itself, (4) heat transfer of the glass window, (5) radiation between the air layer and the surface of the curtain, and most importantly (6) heat transfer and convection between the air layer under cold air infiltration conditions. This section focuses on analyzing the sixth part of the plate of the air layer under the condition of infiltration convection problem, i.e., the calculation formula of the CHTC of a flat air layer under the condition of cold air infiltration is derived by combining the experimental results with theoretical analysis.

**Figure 3.** Calculation diagram of heat transfer coefficient.

Due to the cold air infiltration, the convective heat transfer problem between plates is attributed to the forced convective heat transfer problem. According to the convective heat transfer theory, all CHTC calculations are attributed to the characteristic correlation equations shown in Equations (4) and (5) below

$$Nu = f(Re, Pr) \quad (4)$$

or

$$Nu = cRe^n Pr^m \quad (5)$$

where N_u , P_r , and R_e are dimensionless quantities, which represent Nusselt, Prandtl, and Reynolds numbers, respectively, and c , m , and n are the parameters to be solved. If the value of N_u is less than 1, use $N_u = 1$. According to the law of conservation of energy and the law of heat transfer, N_u and R_e can be determined by Equations (6)–(12), as follows:

$$R_e = \frac{ul}{\nu} \quad (6)$$

$$\phi = C_p m \Delta t = C_p u A_c \rho (t_{out} - t_{in}) \quad (7)$$

$$\phi = h_c A \Delta t_m \quad (8)$$

$$t_w = \frac{1}{2}(t_g + t_c) \quad (9)$$

$$t_f = \frac{1}{2}(t_{out} + t_{in}) \quad (10)$$

$$\Delta t_m = \frac{t_{out} - t_{in}}{\ln \frac{t_m - t_{in}}{t_w - t_{out}}} = \frac{\phi}{h_m A} \quad (11)$$

$$h_c = \frac{\lambda N_u}{d} \quad (12)$$

where u is the average velocity of the air layer, in m/s, obtained by the measuring point; d is the equivalent diameter in m , calculated by formula $d = 4A/P$ (A and P are the area and circumference of the section of the air layer, respectively, measured in m^2 and m , respectively); ν is the coefficient of kinematic viscosity of air, m^2/s ; C_p is constant pressure specific heat capacity, in $KJ \cdot kg^{-1} \cdot K^{-1}$; λ is the coefficient of thermal conductivity, $W \cdot m^{-1} \cdot K^{-1}$; ρ is the density of air, kg/m^3 ; ν , C_p , λ and ρ are based on the average import and export temperature and qualitative temperature; ϕ is the heat flow, representing the heat taken away by the cold air through a section of the air layer in unit time, determined by Equations (5) and (6), measured in W ; ΔT is the air temperature difference at the inlet and outlet, $^{\circ}C$; and ΔT_m is the difference between the average temperature of the wall and the average temperature of the air layer, $^{\circ}C$. T_{in} and T_{out} are the average air temperatures of the inlet and outlet sections respectively, in $^{\circ}C$; T_g and T_c are the average surface temperatures of glass and thermal insulation curtain respectively, in $^{\circ}C$; T_w is the average surface temperature of glass and insulation curtain, in $^{\circ}C$; and T_f is the mean of air layer average temperature, in $^{\circ}C$. A is the surface area of the glass, in m^2 ; A_c is the cross-section area of the air layer, in m^2 , and h_c is the air layer convection heat transfer coefficient to be desired, in $W \cdot m^{-2} \cdot K^{-1}$.

According to Equations (7) and (8), due to the conservation of energy, the h_c in the cavity can be obtained, then the N_u can be obtained according to Equation (12). The parameters c , m , and n that need to be obtained in Equation (4) can be fitted with Matlab software. Finally, the characteristic correlation formula of the air layer formed after laying down the insulation curtain was determined, and the CHTC expression was obtained according to Formula (12).

3.1.1.1. N_u Number Correlations

The 384 groups of experimental data were collated, analyzed, and fitted with Matlab software to obtain the N_u feature correlation formula and applicable scope for SHC/IESW. It was found that under different Reynolds numbers, different function laws are presented as shown below:

$$N_u = 1.68 \times R_e^{0.3} P_r^{0.3} \quad (13)$$

when $R_e < 2300$

$$N_u = 0.03 \times R_e^{0.83} P_r^{0.5} \quad (14)$$

when $2300 > R_e > 10^4$

$$N_u = 0.028 \times R_e^{0.82} P_r^{0.5} \quad (15)$$

when $10^4 > Re > 5 \times 10^4$

$$Nu = 0.03 \times Re^{0.81} Pr^{0.6} \quad (16)$$

when $5 \times 10^4 > Re > 8 \times 10^4$

$$Nu = 0.031 \times Re^{0.78} Pr^{0.7} \quad (17)$$

when $8 \times 10^4 > Re > 15 \times 10^4$

3.1.2. CHTC Calculation Results

After completing the calculation of Nu , the CHTC is calculated according to Equation (12), and then the radiant heat transfer coefficient is determined by Equation (18):

$$h_T = 4\sigma(1/\varepsilon_1 + 1/\varepsilon_2 - 1)^{-1} \times T_f^3 \quad (18)$$

where, h_T is the radiation heat transfer coefficient of glass on both sides of air sandwich, $W \cdot m^{-2} \cdot K^{-1}$; σ is a constant, usually $5.67 \times 10^{-8} W \cdot m^{-2} \cdot K^{-4}$; ε_1 is the calibrated emissivity of external thermal insulation curtain, usually 0.98; ε_2 is the calibrated emissivity of the inner glass surface, usually 0.87, and T_f is the average temperature of the air layer, in $^{\circ}C$.

After the convective and radiative heat transfer coefficients are calculated, the total heat transfer coefficient and thermal resistance of the system can be calculated by using Equations (19) and (20), respectively.

$$h_s = h_c + h_T \quad (19)$$

$$1/h_t = 1/h_s + \delta_1/\lambda_1 + \delta_2/\lambda_2 \quad (20)$$

where, h_s is the total heat transfer coefficient of air interlayer, $W/(m^2 \cdot K)$; $1/h_t$ is the thermal resistance for the entire window, in $(m^2 \cdot c)/W$; δ_1 and δ_2 are the thickness of thermal insulation curtain and glass, both in m, and λ_1 and λ_2 are the thermal conductivity of the thermal insulation curtain and glass, both in $W/(m \cdot c)$. The total heat transfer coefficient can be calculated by Equation (21):

$$1/U = 1/h_o + 1/h_i + 1/h_t \quad (21)$$

where, U is the total heat transfer coefficient of SHC/IESW, $W \cdot m^{-2} \cdot K^{-1}$; h_o is the outdoor CHTC, usually $23 W \cdot m^{-2} \cdot K^{-1}$, and h_i is the indoor CHTC, usually $8.7 W \cdot m^{-2} \cdot K^{-1}$.

During most of the research period, the average outdoor wind speed was 1 m/s, and the outdoor temperature was $-12^{\circ}C$. Therefore, the calculation formula of the Re range of 10,000 to 50,000 was mainly applied; specifically, Equation (12) was used to calculate Nu number and h_c of SHC/IESW. According to Equations (15)–(18), the respective heat transfer coefficients of the four types of energy-saving windows when the window-to-wall ratio is 0.38 are calculated, and the heat transfer coefficient value is $1.71 W \cdot m^{-2} \cdot K^{-1}$.

3.2. Influence of Different Factors on the Convective Heat Transfer between DSF through Simulation

3.2.1. Grid Independence Test

A grid independence test was performed to ensure that the analysis results were not affected by the number of grid variations in the finite element analysis process. The number of grids for A~G, as well as the simulation results, are shown in Table 7.

It is important to note that the number of grids greatly influences the simulation results. When the number of grids is $<50,000$ (A–D), all the detection items showed significantly different values between A, B, C, and D. However, when the number of grids is $>50,000$ (E–G), the simulation results showed minor changes. Basically, the calculation results tend to stabilize after the number of grids increases to a certain magnitude. Thus, the number of grids that meet the independence requirement can be set as 50,000.

Table 7. Results of the grid independence verification.

Item	Grid Number						
	A/10150	B/21090	C/30697	D/41572	E/52220	F/61703	G/72527
T-z-1.1 m (°C)	8.45	8.77	8.97	9.08	9.79	9.8	9.81
T-x-0.8 m (°C)	9.31	9.43	9.51	9.74	10.5	10.6	10.6
T-y-0.5 m (°C)	7.84	8.14	8.37	8.39	8.43	8.44	8.44
T-glass (°C)	5.62	5.76	5.81	5.85	5.92	5.93	5.94

3.2.2. Model Validation

Results from measurements in the experimental room were used to validate the computational model. The numerical validation procedures were designed to fully replicate the experimental work. Figure 4 compares the measured and simulated air temperature at three different vertical positions within the test chamber. The agreement between the measured and modeled temperature profiles in the experimental room was within the acceptable error range.

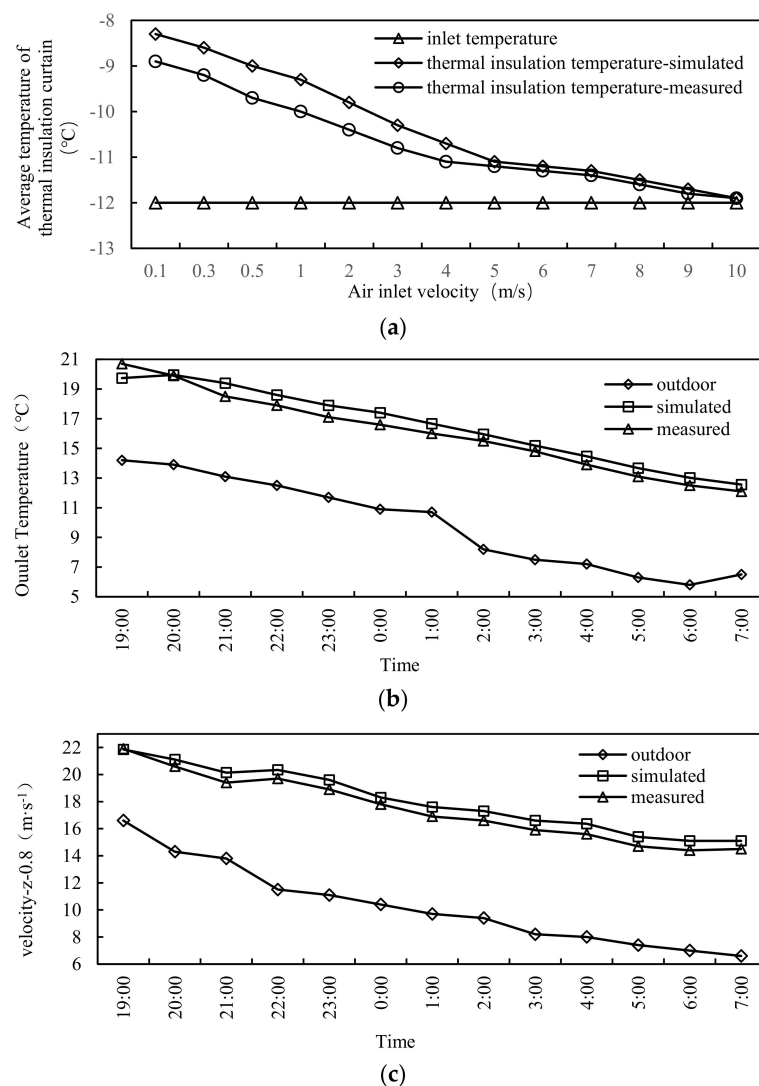


Figure 4. Comparison of simulated and measured temperature profiles: (a) average temperature, (b) outdoor temperature, and (c) velocity.

The simulation results are also shown in the line in Figure 4. It can be seen from the figure that the trend of simulated indoor temperature value is consistent with that of

measured temperature value. The average deviations between the simulated values and the measured values were 2.71, 3.08, 3.63, and 3.07%, and the root mean square errors were 3.05, 4.15, 4.02, and 4.18%, respectively. Therefore, using Fluent software to simulate energy-saving and thermal insulation performance under various working conditions has good reliability.

3.2.3. Analysis of Local Temperature and Wind Speed Values

The temperature and velocity fields between plates with different inlet widths and air layer thicknesses are obtained through simulation analysis. Considering the average temperature at the outlet, the average flow velocity at the section of the air layer, and the average temperature of the thermal insulation curtain as the key analysis parameters, the relationship between them and inlet width and air layer thickness is analyzed. The specific results are shown in Figures 5–7.

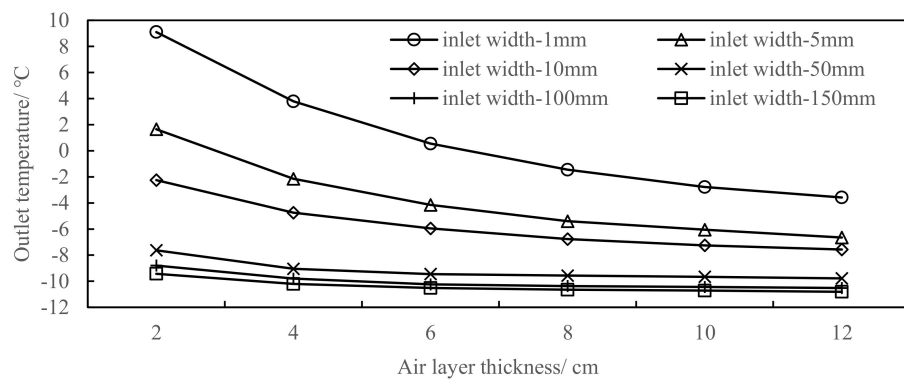


Figure 5. The outlet temperature variation with the thickness of the air layer.

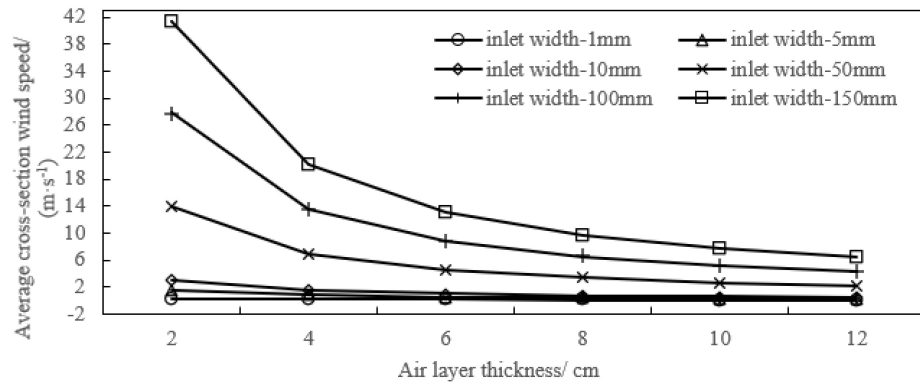


Figure 6. Average cross-section wind speed variation with the thickness of the air layer.

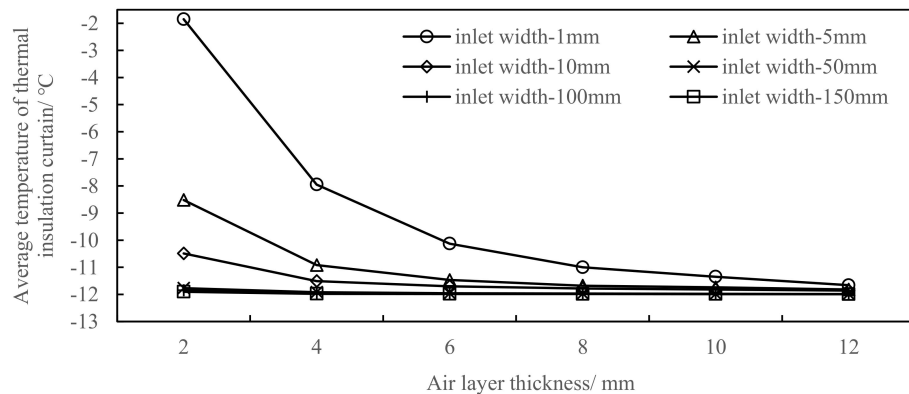


Figure 7. Thermal insulation curtain temperature changes with air layer thickness.

Figure 5 shows the changes in model outlet temperature with air layer thickness under different inlet widths. It is clear that the outlet temperature decreases with the increase of air layer thickness. When the inlet width is 10 mm, the air layer thickness increases from 2 to 12 cm, and the outlet temperature drops from -2.25 to -7.57 °C, accordingly. This is because the thicker the air layer, the greater the air thermal resistance, resulting in less heating loss, so the outlet temperature will be lower. Moreover, the flow velocity of the section decreases with the increase of air layer thickness, the convective heat transfer decreases significantly, and the cold air heats up less, so the outlet temperature will be lower.

In addition, the outlet temperature also decreases with the increase of inlet width. When the air layer thickness is 6 cm, the inlet width increases from 1 to 150 mm, and the outlet temperature correspondingly decreases from 0.55 to -10.52 °C. This is because under the condition of the same air layer thickness and the same inlet wind speed, the larger the inlet width, the larger the cold air flow into the air layer, and the more cold air brought in, so the outlet temperature will be lower.

Figure 6 shows the changes in the average velocity of the middle section of the model with the changes in the thickness of the air layer under different inlet widths. It is clear that the average velocity of the section decreases with the increase of the thickness of the air layer. When the inlet width is 10 mm, the thickness of the air layer increases from 2 to 12 cm. The cross-section wind speed decreases from 2.93 to 0.46 m/s, accordingly. This is because, according to the continuity equation, under the condition of the same inlet width and inlet velocity, the thicker the air layer, the larger the air flow area in the middle section, and the smaller the average velocity of the air layer section.

When the thickness of the air layer is 6 cm, the width of the air inlet increases from 1 to 150 mm, and the velocity of the air inlet increases sharply from 0.11 to $13.2 \text{ m}\cdot\text{s}^{-1}$. This is because under the condition of the same inlet velocity, the larger the inlet width, the more air will flow into the air layer, and under the condition of the same air layer thickness when the flow section area is constant, the average velocity of the air layer increases significantly.

Figure 7 shows the model thermal insulation curtain temperature change with air layer thickness under different inlet widths. It is clear that the thermal insulation curtain temperature decreases with the increase of air layer thickness. When the inlet width is 10 mm, the air layer thickness increases from 2 to 12 cm, and the outlet temperature correspondingly decreases from -10.49 to -11.86 °C. This is because the thicker the air layer, the greater the air thermal resistance; less heat was transferred from hot glass surfaces to the thermal insulation. Moreover, the flow velocity of the section decreases with the increase of air layer thickness, the convective heat transfer decreases significantly, and the heat gain and temperature rise of the insulation curtain is less; so the temperature of the insulation curtain will be lower.

In addition, the temperature of the insulation curtain also decreases with the increase of the inlet width. When the air layer thickness is 6 cm, the inlet width increases from 1 to 150 mm, and the outlet temperature correspondingly decreases from -10.13 to -11.98 °C. This is because under the condition of the same air layer thickness and the same inlet wind speed, the larger the inlet width, the greater the cold air flow into the air layer, and the more cold air brought in (affected by this), the lower the temperature of the insulation curtain.

However, after the thickness of the air layer reaches 100 mm, it can be found that the outlet temperature, air flow rate, and temperature of the thermal insulation curtain all no longer significantly changed. That is, the increase of thermal insulation effect is no longer significant. Combined with the cost and actual installation effect, it is more appropriate when the thickness of the air layer is less than 10 mm.

The analysis of inlet width shows that when the inlet width is 1, 5, and 10 mm, the convective heat transfer intensity does not change significantly. Combined with the actual situation, the smaller the inlet width, the better, as long as an inlet width of equal or less than 1 cm is acceptable.

3.2.4. Contour Analysis of Temperature and Wind Speed

Temperature and wind speed contours of key sections simulated under different air layer thickness (d) conditions and different inlet widths (W_{in}) are respectively intercepted, as shown in Figures 8–11, in order to explore the mechanism and causes behind the laws in Section 3.2.3.

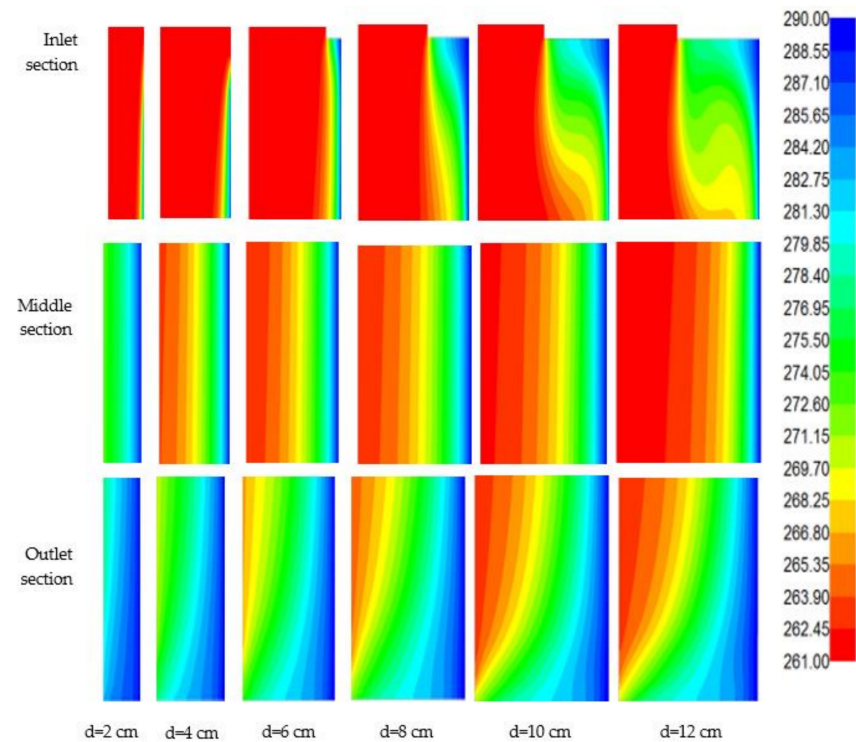


Figure 8. Temperature cloud of cavity variation with the thickness of air layer. (unit: K).

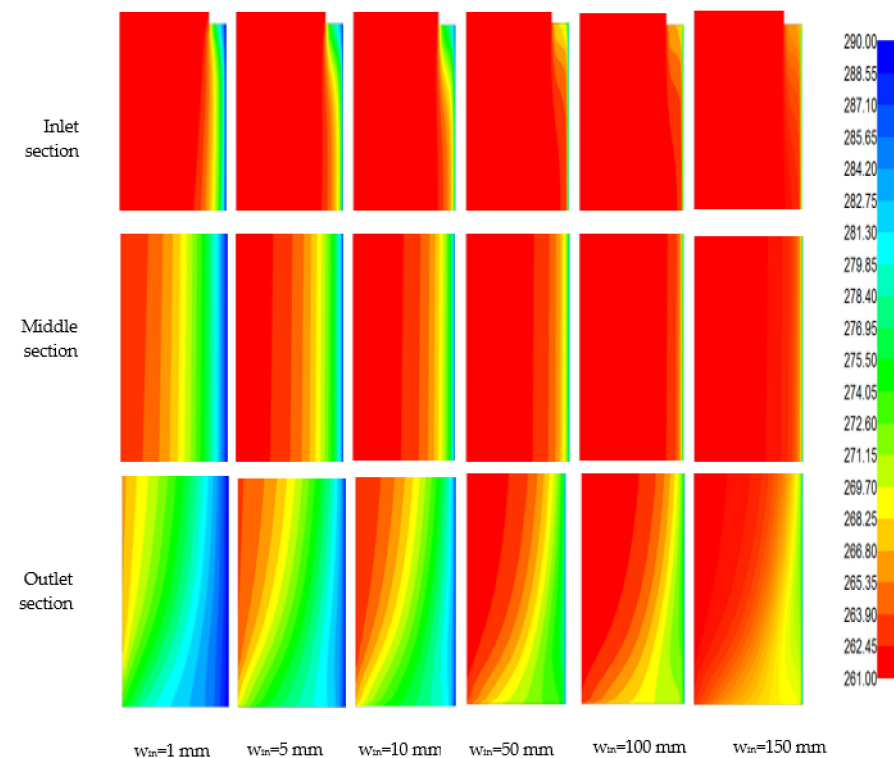


Figure 9. Temperature cloud in the cavity variation with the width of the air inlet (unit: K).

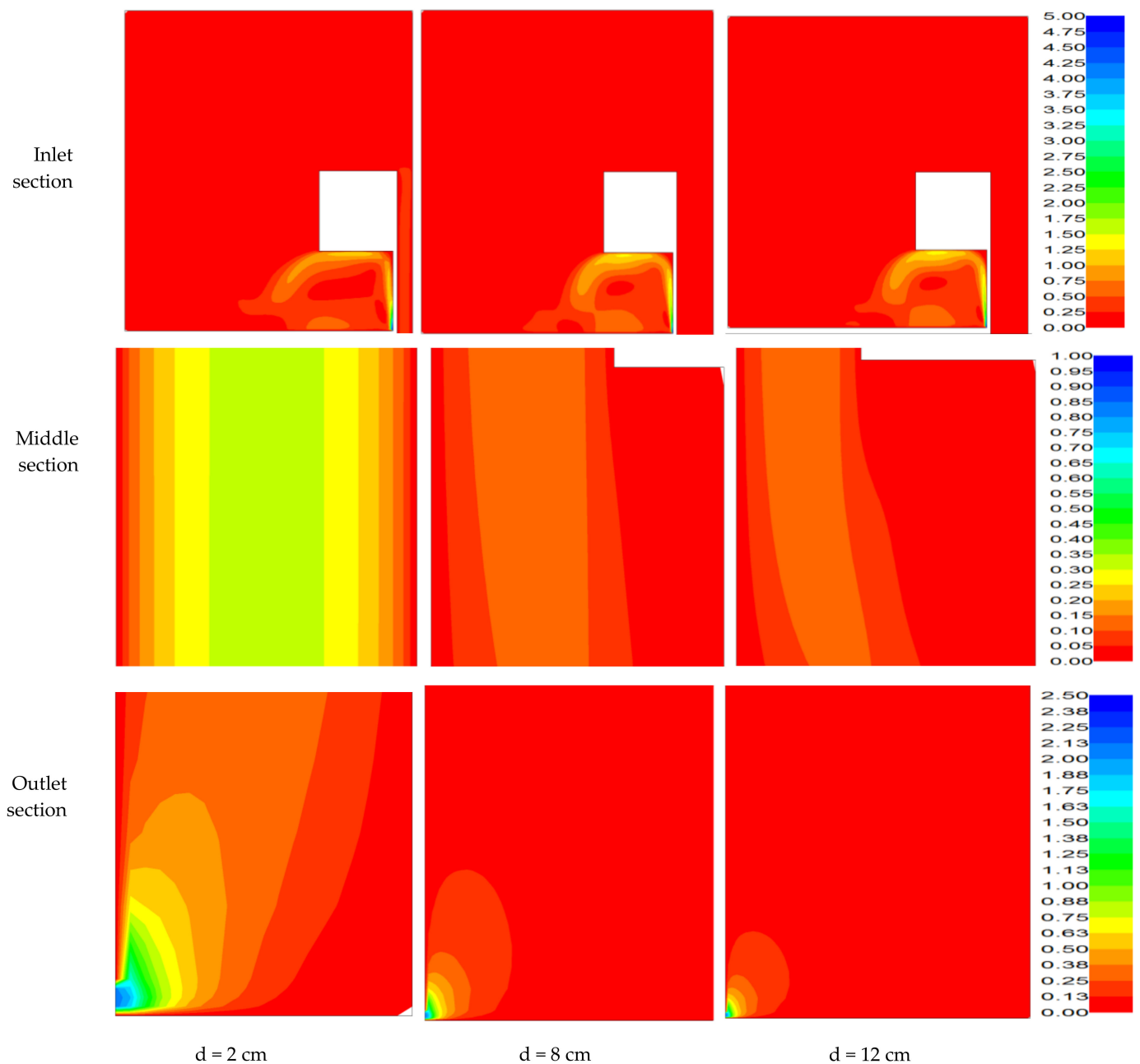


Figure 10. The change of wind velocity cloud in the cavity with air layer thickness.

The simulation contour of wind speed and temperature can be seen to observe and analyze the change rule of temperature field and wind speed field under different inlet widths and different air layer thicknesses, as shown in Figures 8 and 9. The boundary conditions of this simulation are shown in Table 6.

The thermal insulation curtain is placed at night. According to the heat transfer laws, heat transfer between plates is mainly through heat conduction and convection. As can be seen from Figure 8, the entire air layer can be divided into two areas: the discoloration area, and the red area. The discoloration area can be regarded as the area dominated by the conduction from right to left, and the red area can be regarded as the area dominated by the upper and lower convection. As the air layer thickness gradually increases in the order of 2, 4, 6, 8, 10, and 12 cm, the conduction-dominated area and convection-dominated area both gradually expand, and the outlet temperature gradually decreases.

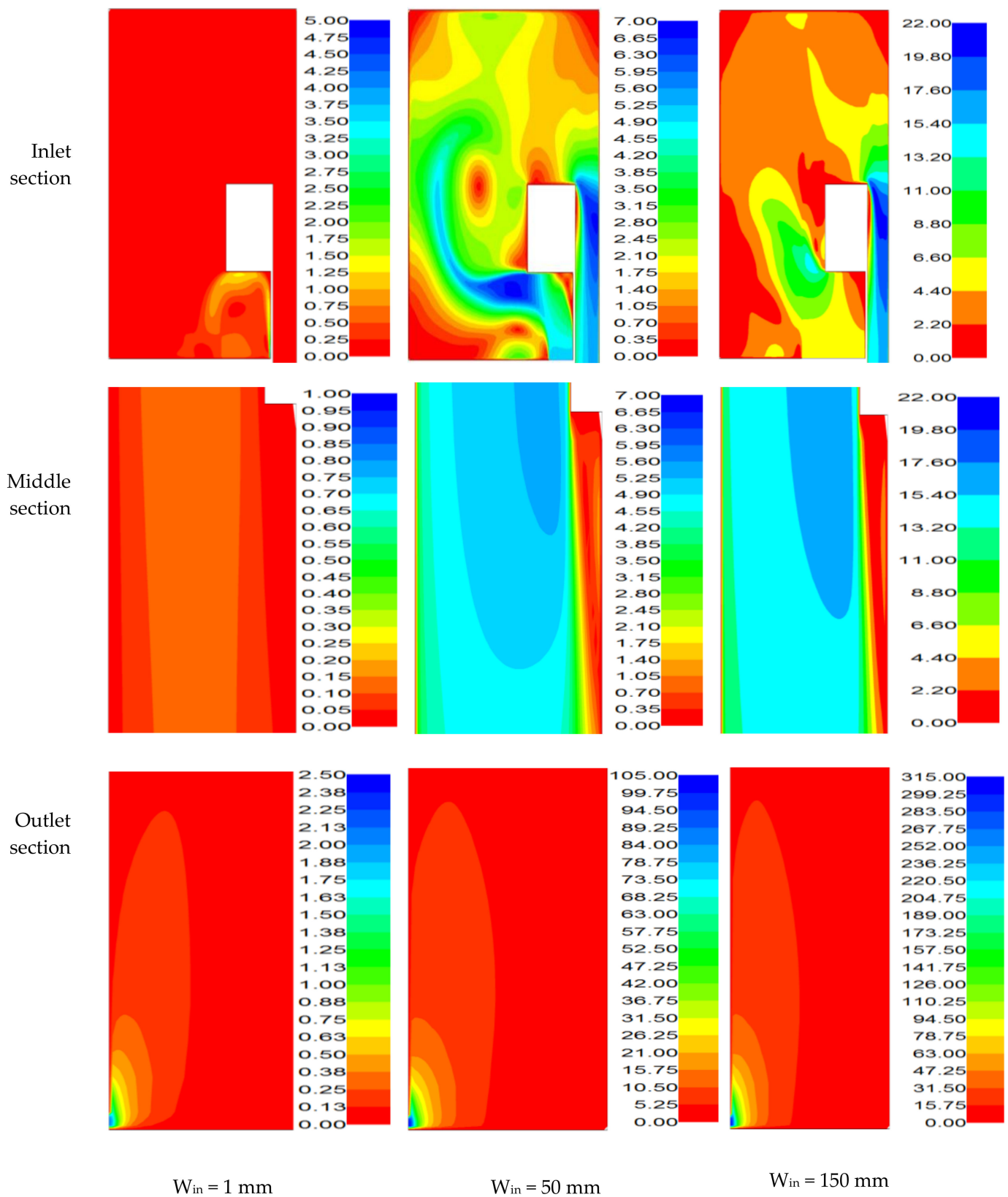


Figure 11. The change of wind speed cloud in the cavity with air inlet width (unit: $\text{m}\cdot\text{s}^{-1}$).

The main reason for this phenomenon is that under the fixed inlet width and inlet velocity, the inlet flow rate is constant; as air layer thickness increases, the entire cavity section average flow velocity decreases, the formation of the corner make air flow resistance increases, which further reduces the air velocity; thus, the convection heat

transfer intensity gradually weakened, and the cold air does not absorb more heat, and the outlet temperature decreases.

Another way to think about it, as the average cavity velocity decreases, the cold air inside the cavity residence time increases, and the heated air quality increases cumulatively, showed difficulties to heats up, and the temperature rise value decreases, so the outlet temperature gradually decreases, which reflects changes in the contour.

In summary, with the increase of the thickness of the air layer, the proportion of the convection dominated area increased but the velocity and intensity reduced, the overall convective heat transfer effect weakened so that the expansion of air layer thickness is beneficial to achieve the thermal insulation effect of the energy-saving windows at night.

Figure 9 shows the influence of different inlet widths on the temperature field cloud in the cavity at 6cm air layer thickness. As the inlet width gradually increases in the order of 1, 5, 10, 50, 100, and 150 mm, the conduction-dominated area gradually shrinks, the convection-dominated area also gradually expands, and the outlet temperature gradually decreases.

The previously mentioned phenomenon occurs because at a constant inlet speed, the inlet width increases, which results in an increase in the inlet area. Then, the inlet cold air flow increases, the quality of the heated cold air continuously increases, the heating difficulty increases, and the temperature rise value decreases, thus, the outlet temperature presents a trend of decrease.

In the vertical direction, with the gradual expansion of the conduction dominated area, the convective dominated area gradually decreases; in the horizontal direction, the convective dominant area obviously expands with the increase of inlet width. Convection speed and intensity gradually increased, but the speed of air heating couldn't catch up with the cold air infiltration rate; thus, the outlet temperature reduced gradually.

In this case, the lower outlet temperature doesn't mean the window has more energy-saving insulation. On the contrary, it means that more cold air is sending the heat out, adding more cold air again. Although the outlet appears to be cooler, it actually takes more heat away. Therefore, increasing the inlet width is harmful to achieving the thermal insulation effect of energy-saving windows at night.

The analysis discussed previously is for the temperature field with different inlet widths and air layer thicknesses. The analysis of the velocity field shown in Figures 10 and 11 is also helpful to analyze the air flow in the cavity of energy-saving windows with different structures; thus, providing a basis for the degree of influence on heat transfer.

Air enters the DSF model shown in Figure 2 from the inlet at a constant speed. Then the air enters the storage box, the air velocity decreases with the larger cross-section area. After that, the air swerves many times with the cross-section area variation and then turns into the cavity, the cross-section is again reduced and became constant, so the air velocity increases again and remains constant. The air continues to flow down to the outlet, since the outlet is only 2 mm wide, the air flows to a significantly higher speed out of the cavity.

Figure 10 shows the flow distribution of the air inside the cavity when the inlet width is 1 mm, and the thickness of the air layer is 2, 8, and 12 cm, respectively.

Horizontally, as the air layer changes from 2 to 8 cm, and then to 12 cm, the air flow at the inlet changes slightly. However, in the middle section, the velocity of the section clearly decreases with the increase of the section area, and the central velocity gradually drops from 0.6 to $0.15 \text{ m}\cdot\text{s}^{-1}$, and then to $0.1 \text{ m}\cdot\text{s}^{-1}$. As the air layer thickens, the air flow forms a vortex, resulting in a maximum velocity of position shift to the left in the cavity, closer to the cold end insulation curtain. The convective heat transfer is further reduced, contributing to lower outlet temperature and air velocity. Therefore, the moderate increase in the thickness of the air layer is beneficial to achieve the heat insulation effect.

Figure 11 shows the air flow distribution in the cavity when the air layer thickness is 6 cm, and the air inlet width is 1, 50, and 150 mm, respectively.

Horizontally, as inlet width increases from 1 to 50 mm, then to 150 mm, a large amount of air enters into the storage box, so the air flow increases, air velocity in the storage box significantly increases, and caused the eddy current effect, vortex area appears in some places. In the middle, as the cross-section area is constant, air section velocity increases with the increase of air flow, and the center of velocity gradually rises from 0.5 to 5 m/s, and then to 14 m·s⁻¹, and then the eddy current effect is diminished, leading to vortex area and maximum flow rate within the cavity position to move to the right, and to be closer to the hot side glass. Therefore, the convective heat transfer will be further strengthened. Furthermore, the air flow increases dramatically, this takes away more heat, which then continues to move in more cold air, and so forth. Therefore, increasing the sealing property of the components and reducing the penetration of cold air is contributing to achieving the heat and thermal insulation effects.

3.2.5. Heat Transfer Coefficient (HTC) under Different Boundary Conditions

Assuming that the average outdoor wind speed is 5 m·s⁻¹, and the outdoor temperature is −12 °C, combined with the model size diagram, the corresponding R_e range is calculated to be 50,000–80,000. The formula $N_{u} = 0.03 \times R_e^{0.81} P_r^{0.6}$, which was presented in Section 3.1.2., is used to calculate the HTC of the SHC/IESW. Using the values from each section in the simulation results, the N_{u} and CHTC of SHC/IESW under different inlet widths and air layer thicknesses are calculated. Then, their HTCs were calculated and listed in Table 8.

Table 8. Heat transfer coefficient value (unit: W·m⁻²·K⁻¹).

Air Layer Thickness/cm	Inlet Width/mm					
	1	5	10	50	100	150
2	1.70	1.81	1.92	2.13	2.21	2.32
4	1.54	1.60	1.66	1.84	1.97	2.06
6	1.50	1.56	1.61	1.76	1.81	1.93
8	1.46	1.52	1.57	1.71	1.75	1.86
10	1.31	1.38	1.42	1.58	1.63	1.69
12	1.28	1.34	1.40	1.56	1.61	1.67

As can be seen from Table 7, even when the wind speed is increased from 1 to 5 m/s, and the window-to-wall ratio is increased from 0.38 to 0.53, the heat transfer coefficient for SHC/IESW of various structures at night in winter is still very low. As mentioned previously, the insulation effect increases with the increase of air layer thickness. When the width of the inlet is the highest and the thickness of the air layer is the lowest, the maximum HTC value is 2.32 W·m⁻²·K⁻¹, but when the width of the inlet is the lowest and the thickness of the air layer is the highest, the HTC value is only 1.28 W·m⁻²·K⁻¹. It can be seen that the insulation effect of SHC/IESW is more noticeable after detailed structural optimization.

4. Conclusions

After the full simulation analysis of the convective heat transfer between DSFs with cold air penetration, the following can be concluded:

- (1) Through the experimental test and the theoretical analysis, the characteristic correlation and heat transfer coefficient of energy-saving windows with different structures are calculated. The N_{u} number correlations under different R_e and P_r numbers are derived. Through the obtained calculation formulas, the heat transfer coefficient of SHC/IESW is 1.71 W·m⁻²·K⁻¹.
- (2) The outlet temperature of the cavity decreases with the increase of the thickness of the air layer and significantly decreases with the increase of the inlet width. When the inlet width is 10 mm, the thickness of the air layer increases from 2 to 12 cm, and the outlet temperature decreases from −2.25 to −7.57 °C. When the air layer thickness is

- 6 cm, the inlet width increases from 1 to 150 mm, and the outlet temperature decreases from 0.55 to -10.52 °C.
- (3) The average cross-section wind speed in the cavity decreases with the increase of air layer thickness and increases with the increase of inlet width. When the inlet width is 10 mm, the thickness of the air layer increases from 2 to 12 cm, and the cross-section wind speed decreases from 2.93 to 0.46 $\text{m}\cdot\text{s}^{-1}$. When the air layer thickness is 6 cm, the inlet width increases from 1 to 150 mm, and the cross-section wind speed increases from 0.11 to 13.2 $\text{m}\cdot\text{s}^{-1}$.
 - (4) The surface temperature of the thermal insulation curtain decreases with the increase of the thickness of the air layer and decreases with the increase of the width of the inlet. When the inlet width is 10 mm, the thickness of the air layer increases from 2 to 12 cm, and the outlet temperature decreases from -10.49 to -11.86 °C. When the air layer thickness is 6 cm, the inlet width increases from 1 to 150 mm, and the outlet temperature decreases correspondingly from -10.13 to -11.98 °C.
 - (5) Under the given boundary conditions, appropriately increasing the thickness of the air layer can help to weaken the convective heat transfer in the cavity, improve the thermal insulation performance of energy-saving thermal insulation windows, and reduce the total heat transfer coefficient to 1.28 – 1.67 $\text{W}\cdot\text{m}^{-2}\cdot\text{K}^{-1}$. Reducing the width of the air inlet is helpful to weaken the convective intensity in the cavity, improve the thermal insulation performance of the energy-saving thermal insulation window, and reduce the total heat transfer coefficient to 1.28 – 1.70 $\text{W}\cdot\text{m}^{-2}\cdot\text{K}^{-1}$.
 - (6) Considering the cost and actual installation effect, the maximum thickness of the air layer is 10 cm; it is acceptable as long as the inlet width is less than 1 cm. Next, SHC/IESW will be installed in different buildings, and their performance under different environmental conditions such as different cities and building orientations will be evaluated and analyzed.

5. Patents

An invention patent named “A utility model relates to a solar energy collecting, shading, energy-saving, and heat preservation window” was granted by the national intellectual property administration of China in 2018. The patent number is ZL 201610854569.3, and the inventors were Qi Tian and Zhiqiang Wang.

Author Contributions: Conceptualization, Z.W. and Q.T.; data curation, J.J.; formal analysis, Z.W.; funding acquisition, Q.T.; investigation, Z.W.; methodology, Z.W.; project administration, Q.T.; resources, Q.T.; software, J.J.; supervision, Q.T.; validation, Z.W.; visualization, J.J.; writing—original draft, Z.W.; writing—review and editing, J.J. and Q.T. All authors have read and agreed to the published version of the manuscript.

Funding: This research was funded by the National 12th Five-Year Science and Technology Support Plan (grant No. 2012BAJ04B02) from the National Natural Science Foundation of China (NSFC), the International Cooperation Project (grant No. 2013DFA61580) from the Ministry of Science and Technology of China (MOST), the National Natural Science Foundation of China (grant No. 51808372), Science and Technology Cooperation and Exchange Project of Shanxi Province (grant No. 202104041101025).

Institutional Review Board Statement: Not applicable.

Informed Consent Statement: Written informed consent has been obtained from the patient(s) to publish this paper.

Data Availability Statement: Data is contained within the article.

Acknowledgments: We gratefully acknowledge the help of Xu Dong, Bin Wu, and Lin Li for the support of the on-site experiments.

Conflicts of Interest: The authors declare no conflict of interest.

Abbreviations

English Symbols:

N_u	Nusselt number
R_e	Reynolds number
$W_{in,out}$	Width of inlet/outlet (mm)
L	Length of inlet/outlet (mm)
P_r	Prandtl number
U	velocity component, x-direction (m/s)
V	velocity component, y-direction (m/s)
U	Overall heat transfer coefficient ($W/m^2 \cdot K$)
Q_{air}	Flow of air infiltration (m^3/s)
G	Acceleration of gravity (m/s^2)
d	Thickness of the cavity (mm)
T, t	Temperature ($^{\circ}C, K$)

Greek Symbols:

Δ	Thickness of the glass/curtain (mm)
ρ	Density (kg/m^3)
Λ	Thermal conductivity ($W/m \cdot K$)

Abbreviations:

SHC/IESW	Solar heat collection/insulation energy-saving window
OW	Ordinary 6 mm glass window
HTC	Heat transfer coefficient
CHTC	Convective heat transfer coefficient
WWR	Window-to-wall ratio
DSF	Double skin façade

References

- Wang, Z.Q.; Tian, Q.; Jia, J. Numerical Study on Performance Optimization of an Energy-Saving Insulated Window. *Sustainability* **2021**, *13*, 935. [[CrossRef](#)]
- Wang, Z.Q.; Akhlaghi, Y.G.; Tian, Q.; Cheng, Y.D. The performance of a novel window with energy-saving potential in cold regions of China. *Indoor Built Environ.* **2022**, *31*, 245–264. [[CrossRef](#)]
- Hong, T.; Kim, J.; Lee, J.; Koo, C.; Park, H.S. Assessment of Seasonal Energy Efficiency Strategies of a Double Skin Façade in a Monsoon Climate Region. *Energies* **2013**, *6*, 4352–4376. [[CrossRef](#)]
- Zhang, T.T.; Yang, H.X. Flow and heat transfer characteristics of natural convection in vertical air channels of double-skin solar façades. *Appl. Energy* **2019**, *242*, 107–120. [[CrossRef](#)]
- Boukendil, M.; Abdelbaki, A.; Zrikem, Z. Numerical simulation of coupled heat transfer through double hollow brick walls: Effects of mortar joint thickness and emissivity. *Appl. Therm. Eng.* **2017**, *125*, 1228–1238. [[CrossRef](#)]
- Kimouche, N.; Mahri, Z.; Saad, A.A.; Popa, C.; Polidori, G.; Maalouf, C. Effect of inclination angle of the adiabatic wall in asymmetrically heated channel on natural convection: Application to double-skin façade design. *J. Build. Eng.* **2017**, *12*, 171–177. [[CrossRef](#)]
- Brandl, D.; Mach, T.; Grobbauer, M.; Hochenauer, C. Analysis of ventilation effects and the thermal behaviour of multifunctional facade elements with 3D CFD models. *Energy Build.* **2014**, *85*, 305–320. [[CrossRef](#)]
- Wang, T.P.; Wang, L.B. A steady heat transfer model of hollow double glazing under entire wave length heat radiation. *Energy Build.* **2014**, *81*, 72–83. [[CrossRef](#)]
- Zhu, Y.Y.; Fan, X.N.; Wang, C.J.; Sang, G.C. Analysis of Heat Transfer and Thermal Environment in a Rural Residential Building for Addressing Energy Poverty. *Appl. Sci.* **2018**, *8*, 2077. [[CrossRef](#)]
- Luo, Y.Q.; Zhang, L.; Liu, Z.B.; Xie, L.; Wang, X.L.; Wu, J. Experimental study and performance evaluation of a PV-blind embedded double skin façade in winter season. *Energy* **2018**, *165*, 326–342. [[CrossRef](#)]
- Urbikain, M.K.; Sala, J.M. Heat transfer through a double-glazed unit with an internal louvered blind: Determination of the thermal transmittance using a biquadratic equation. *Int. J. Heat Mass Tran.* **2012**, *55*, 1226–1235. [[CrossRef](#)]
- Talukdar, D.; Li, C.G.; Tsubokura, M. Numerical investigation of laminar compressible natural convection flow in asymmetrically and isothermally heated open-ended inclined channel. *Int. J. Heat Mass Tran.* **2019**, *130*, 83–97. [[CrossRef](#)]
- Rasheed, A.; Lee, J.W.; Lee, H.W. Development of a model to calculate the overall heat transfer coefficient of greenhouse covers. *Span. J. Agric. Res.* **2017**, *15*, e0208.
- Defraeye, T.; Blocken, B.; Carmeliet, J. Convective heat transfer coefficients for exterior building surfaces: Existing correlations and CFD modelling. *Energy Convers. Manag.* **2011**, *52*, 512–522. [[CrossRef](#)]

15. Sanvicente, E.; Julien, S.G.; Ménézo, C.; Bouia, H. Transitional natural convection flow and heat transfer in an open channel. *Int. J. Therm. Sci.* **2013**, *63*, 87–104. [[CrossRef](#)]
16. Nasri, Z.; Derouch, Y.; Laatar, A.H.; Balti, J. Effect of surface radiation on natural convection in an asymmetrically heated channel-chimney system. *Heat Mass Transf.* **2018**, *54*, 1511–1529. [[CrossRef](#)]
17. Cipriano, J.; Houzeaux, G.; Chemisana, D.; Lodi, C.; Herrero, J.M. Numerical analysis of the most appropriate heat transfer correlations for free ventilated double skin photovoltaic façades. *Appl. Therm. Eng.* **2013**, *57*, 57–68. [[CrossRef](#)]
18. Ioannidis, Z.; Rounis, E.D.; Athienitis, A.; Stathopoulos, T. Double skin facade integrating semi-transparent photovoltaics: Experimental study on forced convection and heat recovery. *Appl. Energy* **2020**, *278*, 115647. [[CrossRef](#)]
19. Agathokleous, R.A.; Kalogirou, S.A. Double skin facades (DSF) and building integrated photovoltaics (BIPV): A review of configurations and heat transfer characteristics. *Renew. Energy* **2016**, *89*, 743–756. [[CrossRef](#)]
20. Inan, T.; Basaran, T.; Ere, A. Experimental and Numerical Investigation of Forced Convection in a Double Skin Façade. *Energies* **2017**, *10*, 1364. [[CrossRef](#)]
21. Kim, E.P. Natural convection characteristics in a vertical open channel with partially heated surfaces. *J. Korean Soc. Mar. Eng.* **2018**, *42*, 635–640.
22. Guo, R.; Heiselberg, P.; Hu, Y.; Johra, H.; Zhang, C.; LundJensen, R.; Jønsson, K.T.; Peng, P. Experimental investigation of convective heat transfer for night cooling with diffuse ceiling ventilation. *Build. Environ.* **2021**, *193*, 107665. [[CrossRef](#)]
23. Cuevas, C.; Fissorea, A.; Fonseca, N. Natural convection at an indoor glazing surface with different window blinds. *Energy Build.* **2010**, *42*, 1685–1691. [[CrossRef](#)]
24. Buonomo, B.; Manca, O. Transient natural convection in a vertical microchannel heated at uniform heat flux. *Int. J. Therm. Sci.* **2012**, *56*, 35–47. [[CrossRef](#)]
25. Popa, C.; Ospir, D.; Fohannoa, S.; Chereches, C. Numerical simulation of dynamical aspects of natural convection flow in a double-skin façade. *Energy Build.* **2012**, *50*, 229–233. [[CrossRef](#)]
26. Zeng, Z.; Li, X.F.; Li, C.; Zhu, Y.X. Modeling ventilation in naturally ventilated double-skin façade with a venetian blind. *Build. Environ.* **2012**, *57*, 1–6. [[CrossRef](#)]
27. Fatnassi, S.; Maad, R.B.; Saad, A.A.; Polidori, G. On the appearance of natural convection induced reversed flow: Precocious hydrodynamic experimental study; Application to PV-DSF systems. *Appl. Therm. Eng.* **2017**, *127*, 1598–1607. [[CrossRef](#)]
28. Jankovic, A.; Goia, F. Impact of double skin facade constructional features on heat transfer and fluid dynamic behaviour. *Build. Environ.* **2021**, *196*, 107796. [[CrossRef](#)]
29. Peng, J.Q.; Lu, L.; Yang, H.X. An experimental study of the thermal performance of a novel photovoltaic double-skin facade in Hong Kong. *Sol. Energy* **2013**, *97*, 293–304. [[CrossRef](#)]
30. Petrichenko, M.R.; Nemova, D.V.; Kotov, E.V.; Tarasova, D.S.; Sergeev, V.V. Ventilated facade integrated with the HVAC system for cold climate. *Mag. Civ. Eng.* **2018**, *77*, 47–58.
31. Velasco, A.; García, S.J.; Guardo, A.; Fontanals, A.; Egusquiza, M. Assessment of the Use of Venetian Blinds as Solar Thermal Collectors in Double Skin Facades in Mediterranean Climates. *Energies* **2017**, *10*, 1825. [[CrossRef](#)]
32. Lau, G.E.; Sanvicente, E.; Yeoha, G.H.; Timchenko, V.; Fossad, M.; Ménézo, C.; Julien, S.G. Modelling of natural convection in vertical and tilted photovoltaic applications. *Energy Build.* **2012**, *55*, 810–822. [[CrossRef](#)]
33. Souza, L.C.O.; Souza, H.A.; Rodrigues, E.F. Experimental and numerical analysis of a naturally ventilated double-skin façade. *Energy Build.* **2018**, *165*, 328–339. [[CrossRef](#)]
34. Jamal, B.; Boukendil, M.; Abdelbaki, A.; Zrikem, Z. Numerical simulation of coupled heat transfer through double solid walls separated by an air layer. *Int. J. Therm. Sci.* **2020**, *156*, 106461. [[CrossRef](#)]
35. Chereches, N.C.; Popovici, C.G.; Cîrlan, V.V.; Hudîşteanu, S.V. Solar protection influence on dynamic insulation efficiency of double skin façades. *E3S Web Conf.* **2019**, *85*, 04003. [[CrossRef](#)]
36. Seo, B.; Yoon, Y.B.; Mun, J.H.; Cho, S. Application of Artificial Neural Network for the Optimum Control of HVAC Systems in Double-Skinned Office Buildings. *Energies* **2019**, *12*, 4754. [[CrossRef](#)]
37. Cho, K.J.; Cho, D.W. Solar Heat Gain Coefficient Analysis of a Slim-Type Double Skin Window System: Using an Experimental and a Simulation Method. *Energies* **2018**, *11*, 115. [[CrossRef](#)]
38. ANSYS Inc. *Ansys-Fluent 14.0 Theory Guide*; ANSYS Inc.: Canonsburg, PA, USA, 2009.